MATERIALS SCIENCE

Facile diamond synthesis from lower diamondoids

Sulgiye Park[1,2], Iwnetim I. Abate[2,3], Jin Liu[1,4], Chenxu Wang[1], Jeremy E. P. Dahl[2], Robert M. K. Carlson[2], Liuxiang Yang[4], Vitali B. Prakapenka[5], Eran Greenberg[5]*, Thomas P. Devereaux[2,3], Chunjing Jia[2], Rodney C. Ewing[1], Wendy L. Mao[1,2], Yu Lin[2†]

Carbon-based nanomaterials have exceptional properties that make them attractive for a variety of technological applications. Here, we report on the use of diamondoids (diamond-like, saturated hydrocarbons) as promising precursors for laser-induced high-pressure, high-temperature diamond synthesis. The lowest pressure and temperature (*P-T*) conditions that yielded diamond were 12 GPa (at ~2000 K) and 900 K (at ~20 GPa), respectively. This represents a substantially reduced transformation barrier compared with diamond synthesis from conventional (hydro)carbon allotropes, owing to the similarities in the structure and full sp^3 hybridization of diamondoids and bulk diamond. At 20 GPa, diamondoid-to-diamond conversion occurs rapidly within <19 µs. Molecular dynamics simulations indicate that once dehydrogenated, the remaining diamondoid carbon cages reconstruct themselves into diamond-like structures at high *P-T*. This study is the first successful mapping of the *P-T* conditions and onset timing of the diamondoid-to-diamond conversion and elucidates the physical and chemical factors that facilitate diamond synthesis.

INTRODUCTION

Diamond has many excellent properties, making it one of the most technologically important materials (*1*). Since the early attempts to synthesize diamond in the 19th century (*2*), there has been a concerted effort to develop efficient approaches and precursors for generating high-quality diamond (e.g., *3–6*). The high energy barrier for direct transformation of carbon precursors to diamond phase often means that a reagent is needed at the expense of purity such as when using high-pressure, high-temperature synthesis, or growth rate has to be compensated as in the case of the chemical vapor deposition (CVD) method (*7, 8*). Designing a new precursor system for facile diamond synthesis that reduces energy and time barrier and understanding the underlying mechanisms would represent a critical advance in diamond synthesis technology.

Diamondoids are the smallest (typically 0.5 to 2 nm) form of hydrogen-terminated carbon cages, which can be superimposed on the diamond lattice. Consisting entirely of sp^3-hybridized bonds, diamondoids combine some of the exceptional properties of bulk diamond and hydrocarbon molecules, such as rigidity, thermal stability, and atomic-level uniformity (*9, 10*). The electronic structure of diamondoids depends on size. The lowest unoccupied molecular orbital (LUMO) stemming from the hydrogen-terminated surface does not shift in energy as a function of diamondoid size, while the highest occupied molecular orbital (HOMO) shifts toward lower energies with decreasing diamondoid size. Hence, adamantane has the largest HOMO-LUMO gap (*11, 12*). Single-cage adamantane has been studied using large volume pressure chambers to form diamond (*3, 13–16*). However, no consensus has emerged on adamantane's behavior at high-pressure, high-temperature conditions, and con-

version mechanisms to nano- and microcrystalline diamonds remain unclear (*13, 14*). Diamondoids were also shown as tenable seeds for CVD diamond growth with pentamantane, which consists of 26 carbon atoms outperforming other diamondoids (*17–19*). While these studies validate the use of diamondoids as promising diamond precursors, a systematic investigation into the pressure-temperature (*P-T*) phase space and mechanistic pathways of diamondoid-to-diamond transformation is lacking. Here, using laser-heated diamond anvil cells (DACs), we explore the diamond synthesis from a full series of lower diamondoids (adamantane $C_{10}H_{16}$, diamantane $C_{14}H_{20}$, and triamantane $C_{18}H_{24}$) without the use of any reagent. Results indicate that lower diamondoids transform to diamond at a substantially reduced energy and temporal barrier compared with other (hydro)carbon materials, with triamantane transforming at the lowest *P-T* boundary. The facile diamond synthesis from lower diamondoids is attributed to their diamond-like structures and sp^3 bonding. The presence of quaternary carbon atoms in triamantane results in convenient conversion by enabling 10–carbon atom cubic diamond cages to form without breaking additional carbon bonds. The findings elucidate the basic properties and mechanistic pathways that govern (hydro)carbon-to-diamond conversion, providing guidance for strategies for energy- and time-efficient diamond synthesis.
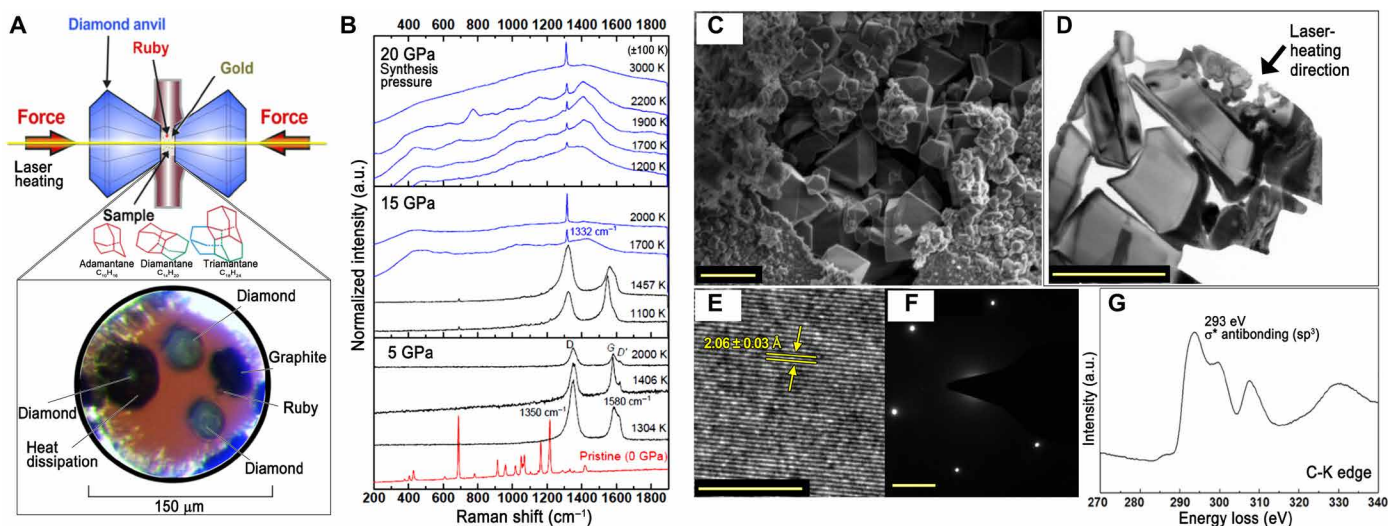
RESULTS AND DISCUSSION

Following laser heating of diamondoids at high pressure, two distinct phases are apparent. Patches of white polycrystalline grains framed by darker surrounding material resulting from partial dissociation indicate diamond, while patches displaying a dark metallic luster indicate graphite (Fig. 1A). Representative Raman spectra of diamantane before, during, and after laser heating at multiple pressures are shown in Fig. 1B (fig. S1 for adamantane and triamantane). When heated to ~1304 K at 5 GPa, the distinguishing vibrational modes of diamantane disappear. The remaining spectrum exhibits two clear bands with Raman shifts at ~1350 and ~1580 cm^{-1}, characteristic of the second- and first-order *D* and *G* bands of graphite, respectively (*20–22*). Even at the highest temperature reached (2000 K) at 5 GPa, no evidence of diamond is observed.

Fig. 1. Identification and characterization of as-synthesized diamond from lower diamondoids. (**A**) Top: Schematic illustration of laser-heated DAC and sample. Bottom: Transmitted light optical image of a sample (inside a DAC) after laser heating. (**B**) Representative Raman spectra of quenched–to–ambient pressure diamantane ($C_{14}H_{20}$) as a function of increasing synthesis temperature at pressures of 5, 15, and 20 GPa. Each Raman spectrum is collected from an individual laser spot with a specific *P-T* value. a.u., arbitrary units. (**C**) Scanning electron microscope (SEM) image of diamond formed from triamantane at 20 GPa and ~2000 K. Well-formed diamond grains are embedded in smaller crystalline diamond grains. (**D**) TEM image of diamond formed from triamantane oriented parallel to the laser-heating beam direction. Scale bars, 1 μm [(C) and (D)]. (**E**) HRTEM image showing the *d*-spacing of diamond (111) plane corresponding to 2.06 ± 0.03 Å. Scale bar, 5 nm. (**F**) Corresponding selected-area electron diffraction pattern with the scale bar of 2 1/nm. (**G**) EELS from a diamond grain representing nearly full sp^3 hybridization of the diamond formed from triamantane (see fig. S3 for SEM and EELS of graphite flake and fig. S4 for energy-dispersive x-ray spectrum of diamond and XRD patterns and SEM images of gold nanoparticles).

At 15 GPa, graphite is still the dominant product when heated to ~1450 K. At a higher temperature of 1700 K, no graphite vibration modes are detected, and a single prominent line with a shift of ~1332 cm^{-1} appears, identified as the first-order Raman peak (T_{2g}) of cubic diamond (*23*). This diamond peak is accompanied by broad, diffuse bands at ~450 to 500, ~700, ~1100, and 1400 to 1500 cm^{-1}. The three diffuse bands at lower Raman shifts could arise from a pressure-induced amorphous phase from diamantane, but its structural periodicity is eliminated by compression. The diffuse band at ~1400 to 1500 cm^{-1} can stem from diamond-like hydrocarbon, with sp^3 carbon networks embedded within the crystalline cubic diamond. At 20 GPa, diamond is the dominant product in the temperature range of ~1200 to 2200 K, and no sign of graphite is observed. Broad diffuse Raman bands at ~1400 to 1500 cm^{-1} persist at this pressure for temperatures ranging from 1200 to 2200 K, suggesting that hydrogenated diamond-like amorphous carbon forms alongside diamond unless the kinetic barrier of the phase transition is overcome by increased laser-heating duration or higher temperature. The observed diamondoid-to-diamond phase transition is a direct process in that it is not preceded by graphite formation. This was experimentally tested by first forming graphite from diamondoids at a lower *T* and applying the same *P-T* conditions on the graphite as those applied for forming diamond from diamondoids. None of the graphite transitioned into diamond at these *P-T* conditions, comparable to those at which diamondoids directly transitioned to diamond.

There is no detectable signal of hydrogen radicals or dihydrogen molecules following the formation of graphite or diamond. However, spatially resolved Raman spectra exhibit vibrational modes that are typical of doubly bonded carbon at Raman bands around ~3080 cm^{-1}, possibly indicating partial carbon polymerization (fig. S2) (*24*). Hydrogen may form following dehydrogenation [as indicated in ab initio molecular dynamics (AIMD) simulations] and escape

from the sample chamber upon quenching. We also did not observe photoluminescence associated with nitrogen vacancy centers in the recovered diamond. This may be attributed to the swift diamondoid-to-diamond conversion that does not allow sufficient time for the vacancy to migrate adjacent to the nitrogen impurity or to the reduced temperature threshold for diamond formation that prevents the vacancy from being mobile.

Representative images of diamond crystals formed from triamantane at 20 GPa and 2000 K are shown in Fig. 1 (C to F). At the center of the laser beam are coarse-grained, well-faceted euhedral diamond crystals that are loosely attached and embedded in a cryptocrystalline diamond matrix. The monocrystalline diamond formed from lower diamondoids has an octahedral form. The sample cut perpendicular to the surface reveals a variation of diamond size along the thermal gradient of the laser heating (Fig. 1D). There is a sharp transition from anhedral, cryptocrystalline, small (~54 ± 5 nm) diamond grains to euhedral, large (~1.1 ± 0.2 μm) single crystals as a function of sample depth. The overall diamond size ranges from tens of nanometers to ~4 μm. The spatial variation in morphology and size indicates the sensitivity of the transformation in diamondoids to temperature.

High-resolution transmission electron microscopy (HRTEM) images of diamond formed from triamantane exhibit an average *d*-spacing of 2.06 ± 0.03 Å, consistent with the (111) plane of cubic diamond (Fig. 1E). An electron energy loss spectrum (EELS) from the same region exhibits a peak in the near-edge structure at 293 eV, representative of the σ* orbital of the sp^3 carbon (Fig. 1G) and consistent with a diamond carbon *K*-edge. A small peak at 286 eV corresponds to the π* orbital of the sp^2 carbon and is attributed to a minute fraction of diamond-like amorphous carbon, residual diamondoid, or surface CH (*25*). These results confirm that diamond is the major phase formed from lower diamondoids at 20 GPa.
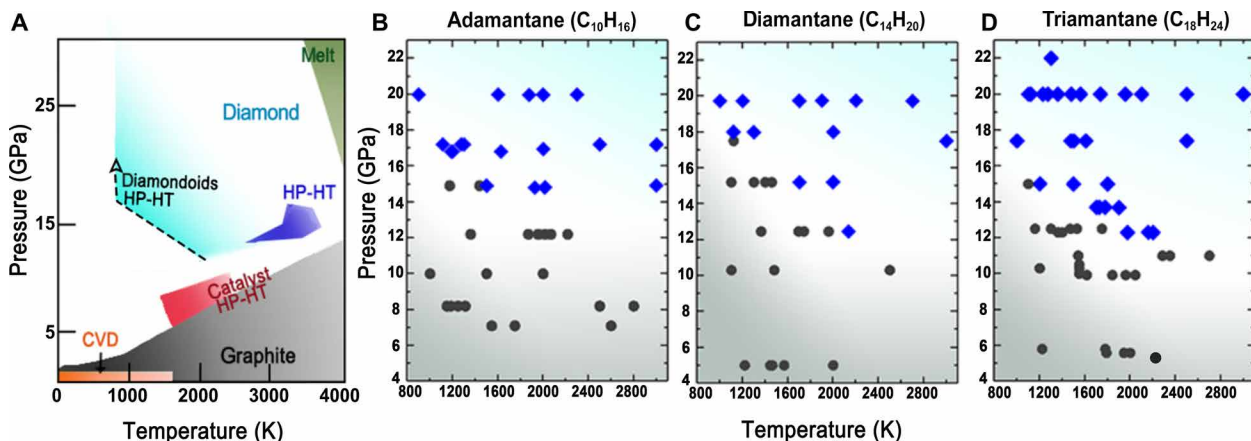
Fig. 2. *P-T* synthesis diagrams of lower diamondoids. (**A**) *P-T* range in which diamond forms from lower diamondoids compared with conventional carbon materials using various synthesis techniques (*6*). HP-HT in the graph represents high-pressure, high-temperature diamond synthesis from laser heating at high pressure or multi-anvil apparatus. Catalyst HP-HT refers to diamond formed with the assistance of reagents/catalysts. The black dashed lines represent regions of diamond synthesis from diamondoids based on this work. (**B** to **D**) *P-T* synthesis diagrams of diamond versus graphite formation from adamantane, diamantane, and triamantane.
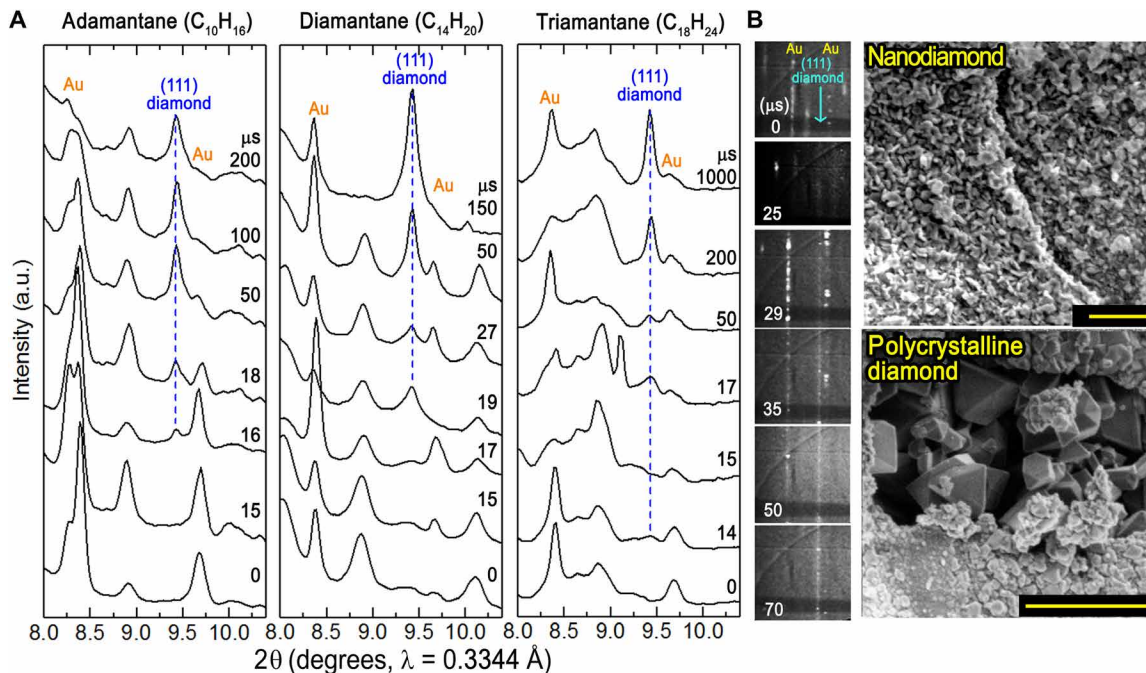
Fig. 3. Onset timing of diamond formation from lower diamondoids. (**A**) In situ XRD patterns of three diamondoids as a function of increasing laser-heating duration. Nonlabeled peaks belong to the sample. (**B**) Cake integration of two-dimensional diffraction images highlighting the texture of diamond growth as a function of increasing laser-heating time. Representative SEM images of nanodiamond and polycrystalline diamond. Scale bars, 2 μm.

Compared with conventional carbon materials such as graphite, the *P-T* synthesis diagrams for the three lower diamondoids (Fig. 2) exhibit a much lowered temperature threshold for diamond formation by >1000 K at a comparable pressure (~12 to 15 GPa) (*26*, *27*). This is especially true given that the lower bound portrayed in this work is a temperature at which diamondoids had transformed to ~100% diamond, given the extreme sensitivity of Raman spectroscopy to sp²-hybridized carbon (*28*, *29*). Among the three diamondoids tested, triamantane requires the lowest temperature for diamond formation at a given pressure.

The onset timing of diamond formation was further examined by controlling the laser heating duration. In situ x-ray diffraction (XRD) patterns at 20 GPa show the appearance of the diamond (111) peak at 16, 19, and 14 μs for adamantane, diamantane, and triamantane, respectively (Fig. 3A). The general kinetic trend follows the diamond formation temperature; the material with the lowest required *P-T*, triamantane, has the fastest transition time, followed by adamantane and diamantane. Qualitative analysis of the diamond particle size using two-dimensional XRD indicates an increasing diamond grain size with an increasing laser-heating time (Fig. 3B).
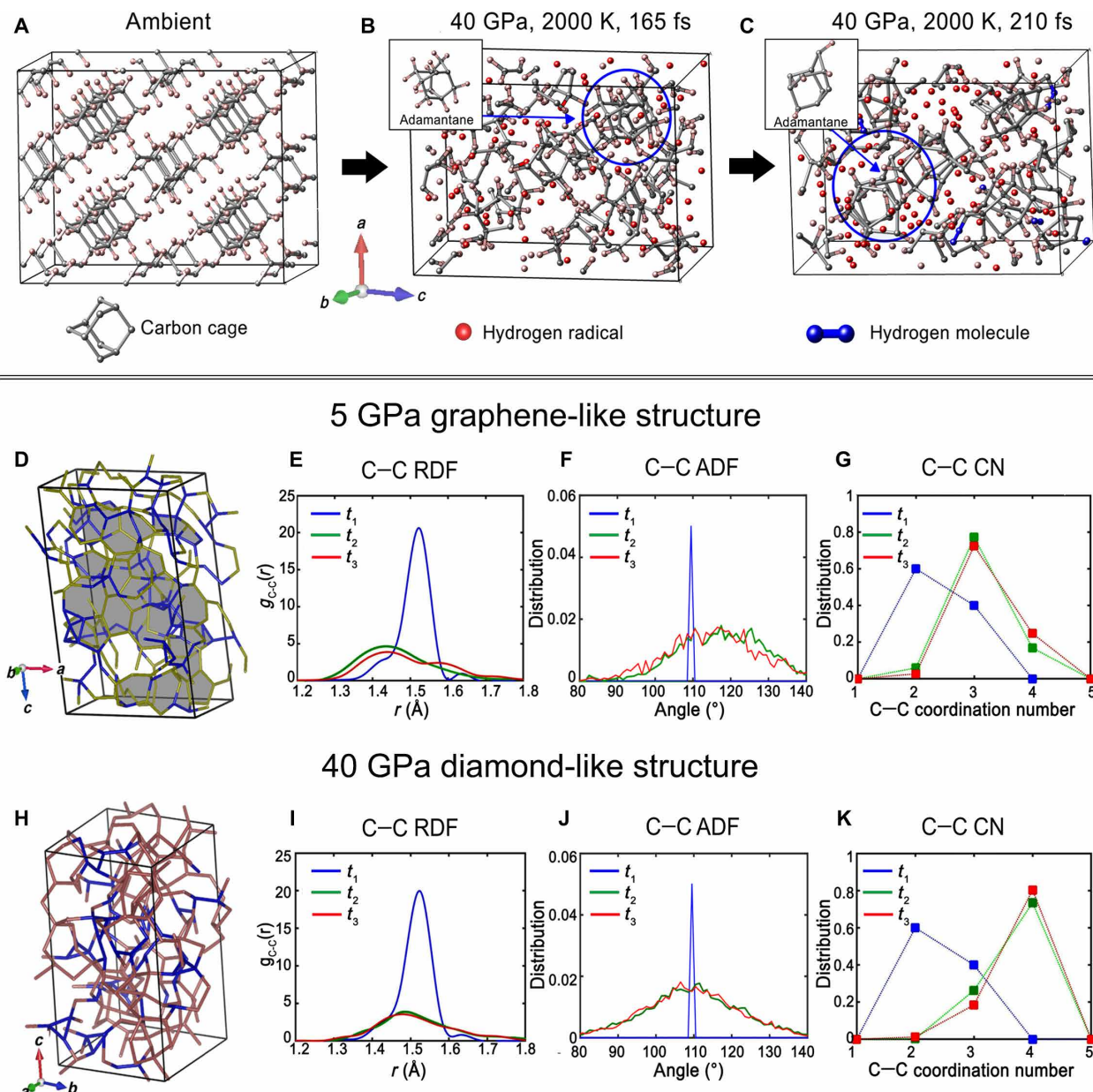
Fig. 4. AIMD simulations for elucidating adamantane-to-diamond transformations. (**A**) Pristine adamantane unit cell. (**B**) Dehydrogenation of adamantane following 165 fs at 40 GPa and 2000 K. There is 28% H radical formation. The inset represents a pristine adamantane cage that has not yet been ruptured. (**C**) Dehydrogenation of adamantane following 215 fs at 40 GPa and 2000 K. Approximately 37% H radicals and 5% dihydrogen molecules are formed. The inset is a slightly distorted yet still a fully intact adamantane cage. The captured dehydrogenation processes are all metastable moments before full relaxation. The H–H bond distance cutoff was 0.851 Å. (**D**) Fully relaxed structure of adamantane at 5 GPa and 2000 K at t_3. While the layers are not structurally in plane, graphene-like features are clearly observed as indicated by gray shaded areas. (**E** to **G**) C–C RDF, ADF, and CN of adamantane at 5 GPa and 2000 K. (**H**) Fully relaxed structure of adamantane at 40 GPa and 2000 K at t_3. Colored in pink are the carbon atoms with fourfold coordination. (**I** to **K**) C–C RDF, ADF, and CN of adamantane at 40 GPa and 2000 K. The H-free systems were simulated for 9 ps. t_1, t_2, and t_3 represent 0, 4, and 9 ps, respectively.

This is evidenced by a gradual transition from a faint and broad diffraction line, typical of nanometer-sized diamond, to narrow and spotty lines at longer times, characteristic of grain growth in polycrystalline diamond.

AIMD simulations support the experimental results and confirm the diamondoid-to-diamond transformation pathway. When exposed to high *P-T*, adamantane first undergoes dehydrogenation (Fig. 4, A to C). After 165 fs, partial rupturing of C–H bonds leads

to ~28% H radical formation, but there are still traces of intact adamantane units. The radicals bond with each other and form hydrogen molecules by 210 fs (Fig. 4C). To carefully trace the sequential steps of diamond formation and to reduce computational cost, further calculations were performed on bare carbon cages by removing all hydrogen atoms. After 9 ps, the following changes are observed. At 5 GPa and 2000 K, H-free adamantane experiences a partial bond rupture and the remaining cyclic carbons share edges to form
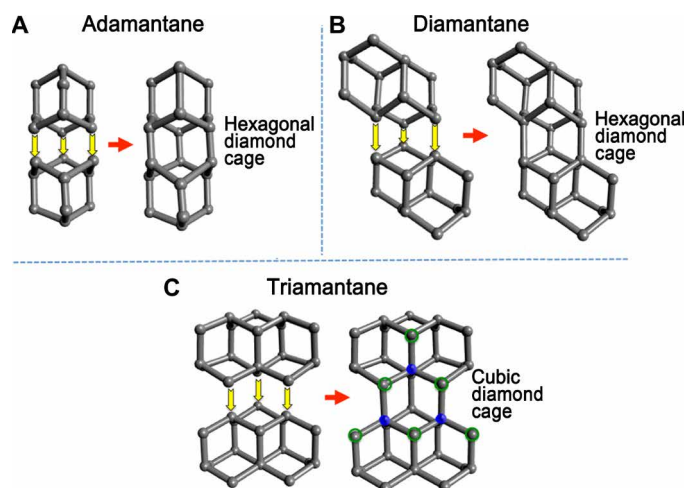
Fig. 5. Mechanisms of diamond formation from lower diamondoids. (**A**) Two unpassivated adamantane molecules can only fuse to form a hexagonal diamond cage. (**B**) Two unpassivated diamantane molecules can only fuse to form a hexagonal diamond cage. (**C**) Two unpassivated triamantane molecules fuse to form a cubic diamond cage enabled by the quaternary carbon atoms (blue spheres) and surrounding tertiary carbon atoms (circled in green).

randomly oriented graphene layers (Fig. 4D and fig. S5). Carbon atoms (63%) have threefold coordination indicating phase transformation into graphite. Analysis of both the radial distribution function (RDF) of the C–C bond length and the angular distribution function (ADF) of the C–C–C angle accompanies the structural transformation (Fig. 4, E to G, and fig. S6). At 5 GPa, C–C RDF exhibits a shift from 1.54 to 1.42 Å, and C–C–C ADF shifts from 109.5° to 120°, resembling those of a graphite structure. Concurrently, the C–C coordination number (CN) shows an increase in the threefold coordination and a decrease of the twofold coordination, typical of the graphite-like feature. At an elevated pressure of 40 GPa, 80% carbon atoms have fourfold coordination (Fig. 4H and fig. S5), indicating a shift to a diamond-like structure. The RDF and ADF of the adamantane remain at 1.54 Å and 109.5°, respectively, while the C–C coordination shifts to four, all of which is consistent with diamond formation (Fig. 4, I to K, and fig. S6).

The reduced energy barrier for diamond formation from lower diamondoids compared with conventional carbon allotropes is attributed to the similarity of the diamondoid structure and bonding with that of the bulk diamond. Full sp^3 hybridization, highly symmetric and strain-free structures, C–C frameworks that are superimposable on the diamond lattice, and intrinsic intramolecular covalent bonds all combine to lower the activation and kinetic barrier required to form diamond. AIMD calculations further support the idea that diamondoids hold a certain "memory" of the bulk diamond structure at high *P-T*, indicated by the remnants of intact carbon cages (Fig. 4, B and C). To attest for the bulk diamond-like features in facilitating facile diamondoid-to-diamond synthesis, further experiments were conducted on octadecane with full sp^3 hybridization, which confirmed that higher temperatures were necessary for diamond formation (fig. S7).

Among the lower diamondoids tested, triamantane stands out with the lowest *P-T* required for diamond formation. Differences in the ease of forming diamond from lower diamondoids appear to arise from differences in the potential ability of their dehydrogenated

carbon frameworks to polymerize and form an extended cubic diamond structure. While at least three specifically oriented carbon frameworks are required for adamantane and diamantane to form a cubic diamond structure, only two triamantane carbon frameworks need to be linked and no breaking of C–C bonds is required within the independent triamantane structures. This is facilitated by the presence of quaternary carbon atoms and surrounding tertiary carbon atoms within the triamantane structure, which have the potential to form 10–carbon atom cubic diamond cages without breaking carbon bonds. Condensed triamantane dimers provide superior seed structures with the potential to grow into extended cubic diamond (Fig. 5).

CONCLUSIONS AND OUTLOOK

These findings show that diamondoids are promising candidates for diamond synthesis. They offer an energetically superior pathway to form diamond on the order of microsecond without the addition of any reagent that can adversely affect the purity of the resulting diamond. The results also elucidate the basic properties and mechanistic pathways that affect the facile (hydro)carbon-to-diamond conversion, including the diamond-like structures and bonding, as well as quaternary carbon atoms that enable a swift conversion. The facile synthesis of diamond suggests a promising use of diamondoids for investigating light-emitting defects in diamonds, which is of interest in the fields ranging from quantum technologies to biological sciences (*30–32*). Doped or functionalized with targeted defect elements, these energy- and time-efficient precursors can lead to better understanding and discovery of color center–containing diamonds.

MATERIALS AND METHODS

High *P-T* experiments were performed using laser-heated DACs at beamlines 16-ID-B and 13-ID-D of the Advanced Photon Source (APS), Argonne National Laboratory (ANL) (Nd: YLF laser); beamline 12.2.2 of the Advanced Light Source (ALS), Berkeley National Laboratory (BNL) (Nd:YLF laser); and the High Pressure Synergetic Center (HPSynC) at APS, ANL (Nd:YAG laser).

Standard symmetric DACs, each with a pair of 300- to 500-μm culet diamonds, were used to generate pressures up to ~20 GPa. Tungsten gaskets were indented to a thickness of 30 to 60 μm, and a hole with a diameter of 150 to 300 μm was drilled in the center to serve as a sample chamber. For all samples, less than 3 weight % Au powder that is not catalytic or reactive with the samples was mixed to serve as a laser absorber. Pressure in the DAC was determined using the standard ruby fluorescence and Au equation of state (*33*). Once a target pressure was reached, continuous double-sided laser heating (λ = 1064 nm) was used to heat the sample in the DAC. The flat top beam size was ~15 μm × 15 μm, and the laser output power had a stability better than ±1%, which yields errors of less than 100 K in temperature (*34*). The temperature was measured at the center of the laser spot by analyzing the pyrometric signal emitted by a 6 μm × 6 μm area. To probe the onset timing of diamond formation and the effect of laser heating duration on diamond grain growth, a microsecond pulsed laser-heating technique was used at GeoSoilEnviroCARS beamline 13-ID-D (APS). A frequency-modulated laser beam with a pulse width of 1 μs was synchronized with the x-ray source and a time-gated detector, and a few laser pulses were accumulated

at a rate of 10 kHz for each measurement for high-quality XRD data (*35*).

After laser heating at various pressures, the formation of graphite and diamond was observed using optical microscopy. Further analysis of the laser-heated spots was conducted using Raman spectroscopy. To avoid the high-intensity diamond signal from the DACs, the gaskets with samples were removed from the cells before analysis. Raman spectra were collected using a Renishaw InVia system with a λ = 514.5 nm laser source.

Recovered products were further analyzed using SEM (scanning electron microscope) and TEM. Samples were prepared using a focused-ion beam operating with Ga^+ ions at 5-kV accelerating voltage. Milled sections were imaged using an FEI Tecnai operating at 200 kV. Electron diffraction images, HRTEM images, and EELS data were then obtained using a Gatan digital micrograph.

AIMD calculations, as implemented in the Vienna Ab Initio Simulation Package (VASP), were performed to shed light on the mechanisms of diamondoid-to-diamond conversion (*36*). Projector augmented wave potentials (*37*) were used to mimic the ionic cores, while the generalized gradient approximation in the Perdew-Burke-Ernzerhof flavor was used for the exchange and correlation functional (*38*). Optimized atomic coordinates and lattice parameters of adamantane were obtained from the experimental XRD. For the reasons described in the discussion section, the simulation was performed on bare adamantane C–C cages of a $2 \times 2 \times 2$ supercell with a total of 160 atoms with isothermal-isobaric ensemble. For all calculations, plane waves with a kinetic energy up to 800 eV were used to expand the wave functions, and the Brillouin zone was sampled by a $2 \times 2 \times 1$ Monkhorst-Pack k-point mesh (*39*). Energy convergence was assumed when the energy difference between the self-consistent cycles was less than 10^{-4} eV. For each simulation, the C–C adamantane framework was subjected to 5, 20, and 40 GPa. A temperature of 2000 K was set for each relaxed structure. For all three pressures, the calculation was performed for 9 ps, at which point the RDF stopped evolving, with a 1.5-fs time step. C–C CN, as well as RDF and ADF, was captured at a consequent time frame to constrain the phase transformation pathway. To sustain both the temperature and pressure of the system via Langevin dynamics, friction coefficients of 10 ps^{-1} for atoms and 5 ps^{-1} (fictitious mass of 500 atomic mass units) for lattice degrees of freedom were used. The temperature oscillations were controlled every 40 time steps. Virtual NanoLab software was used to calculate CN, RDF, and ADF. CN and RDF were calculated by integrating 30 time steps around t_1, t_2, or t_3. ADF was calculated at a single snapshot of t_1, t_2, or t_3.

SUPPLEMENTARY MATERIALS
Supplementary material for this article is available at http://advances.sciencemag.org/cgi/content/full/6/8/eaay9405/DC1

Fig. S1. Representative Raman spectra of quenched products after laser-heating adamantane and triamantane at pressures of 5, 15, and 20 GPa.
Fig. S2. Higher Raman frequency of adamantane compressed and heated to 10 GPa and ~2000 K.
Fig. S3. Characterization of graphite formed from diamondoids.
Fig. S4. XRD and SEM data of gold nanoparticles and energy-dispersive x-ray spectrum of diamond.
Fig. S5. Structural evolution of dehydrogenated adamantane at 5 and 40 GPa and 2000 K.
Fig. S6. False color plots indicating the calculated RDFs as a function of structural evolution time at 5 and 40 GPa.
Fig. S7. Representative Raman spectra of quenched samples after laser-heating octadecane at the synthesis pressure of 12.5 GPa.

REFERENCES AND NOTES

1. W. H. Taylor, Structure and properties of diamond. *Nature* **159**, 729–731 (1947).
2. J. B. Hannay, Artificial diamonds. *Nature* **22**, 241 (1880).
3. A. Onodera, K. Suito, Y. Morigami, High-pressure synthesis of diamond from organic compounds. *Proc. Jpn. Acad. Ser. B Phys. Biol. Sci.* **68**, 167–171 (1992).
4. J.-Y. Choi, K. Y. Eun, J.-S. Kim, S.-J. L. Kang, Effect of carbon crystallinity on the nucleation and growth of diamond under high pressure and high temperature. *Diamond Relat. Mater.* **7**, 1196–1200 (1998).
5. N. V. Novikov, New trends in high-pressure synthesis of diamond. *Diamond Relat. Mater.* **8**, 1427–1432 (1999).
6. F. P. Bundy, W. A. Bassett, M. S. Weathers, R. J. Hemley, H. U. Mao, A. F. Goncharov, The pressure-temperature phase and transformation diagram for carbon; updated through 1994. *Carbon* **34**, 141–153 (1996).
7. B. V. Spitsyn, L. L. Bouilov, B. V. Derjaguin, Vapor growth of diamond on diamond and other surfaces. *J. Cryst. Growth* **52**, 219–226 (1981).
8. S. J. Lv, S. M. Hong, C. S. Yuan, Y. Hu, Selenium and tellurium: Elemental catalysts for conversion of graphite to diamond under high pressure and temperature. *Appl. Phys. Lett.* **95**, 242105 (2009).
9. S. Stauss, K. Terashima, *Diamondoids: Synthesis, Properties and Applications* (CRC Press, ed. 1, 2017).
10. A. T. Balaban, P. VonRagé Schleyer, Systematic classification and nomenclature of diamond hydrocarbons—I: Graph-theoretical enumeration of polymantanes. *Tetrahedron* **34**, 3599–3609 (1978).
11. T. M. Willey, C. Bostedt, T. van Buuren, J. E. Dahl, S. G. Liu, R. M. Carlson, L. J. Terminello, T. Möller, Molecular limits to the quantum confinement model in diamond clusters. *Phys. Rev. Lett.* **95**, 113401 (2005).
12. T. M. Willey, C. Bostedt, T. van Buuren, J. E. Dahl, S. G. Liu, R. M. K. Carlson, R. W. Meulenberg, E. J. Nelson, L. J. Terminello, Observation of quantum confinement in the occupied states of diamond clusters. *Phys. Rev. B* **74**, 205432 (2006).
13. V. A. Davydov, A. V. Rakhmanina, V. Agafonov, B. Narymbetov, J.-P. Boudou, H. Szwarc, Conversion of polycyclic aromatic hydrocarbons to graphite and diamond at high pressures. *Carbon* **49**, 9981–9885 (2005).
14. E. A. Ekimov, O. S. Kudryavtsev, N. E. Mordvinova, O. I. Lebedev, I. I. Vlasov, High-pressure synthesis of nanodiamonds from adamantane: Myth or reality? *Chem. Nano. Mat.* **4**, 269–273 (2018).
15. R. H. Wentorf Jr., The behavior of some carbonaceous materials at very high pressures and high temperatures. *J. Phys. Chem.* **69**, 3063–3069 (1965).
16. E. A. Ekimov, K. M. Kondrina, N. E. Mordvinova, O. I. Lebedev, D. G. Pasternak, I. I. Vlasov, High-pressure, high-temperature synthesis of nanodiamond from Adamantane. *Inorg. Mater.* **55**, 437–442 (2019).
17. Y.-K. Tzeng, J. L. Zhang, H. Lu, H. Ishiwata, J. Dahl, R. M. K. Carlson, H. Yan, P. R. Schreiner, J. Vučković, Z.-X. Shen, N. Melosh, S. Chu, Vertical-substrate MPCVD epitaxial nanodiamond growth. *Nano Lett.* **17**, 1489–1495 (2017).
18. J. E. P. Dahl, J. M. Moldowan, Z. Wei, P. A. Lipton, P. Denisevich, R. Gat, S. Liu, P. R. Schreiner, R. M. K. Carlson, Synthesis of higher diamondoids and implications for their formation in petroleum. *Angew. Chem.. Int. Ed.* **49**, 9881–9885 (2010).
19. M. A. Gebbie, H. Ishiwata, P. J. McQuade, V. Petrak, A. Taylor, C. Freiwald, J. E. Dahl, R. M. K. Carlson, A. A. Fokin, P. R. Schreiner, Z.-X. Shen, M. Nesladek, N. A. Melosh, Experimental measurement of the diamond nucleation landscape reveals classical and nonclassical features. *Proc. Natl. Acad. Sci. U.S.A.* **115**, 8284–8289 (2018).
20. S. Reich, C. Thomsen, Raman spectroscopy of graphite. *Philos. Trans. R. Soc. A* **362**, 2271–2288 (2004).
21. Y. Kawashima, G. Katagiri, Fundamentals, overtones, and combinations in the Raman spectrum of graphite. *Phys. Rev. B* **52**, 10053–10059 (1995).
22. C. Thomsen, S. Reich, Double resonant Raman scattering in graphite. *Phys. Rev. Lett.* **85**, 5214–5217 (2000).
23. J. Filik, J. N. Harvey, N. L. Allan, P. W. May, J. E. P. Dahl, S. Liu, R. M. K. Carlson, Raman spectroscopy of nanocrystalline diamond: An ab initio approach. *Phys. Rev. B* **74**, 035423 (2006).
24. N. Zhang, Z. J. Tian, Y. Y. Leng, H. T. Wang, F. Q. Song, J. H. Meng, Raman characteristics of hydrocarbon and hydrocarbon inclusions. *Sci. China Ser. D Earth Sci.* **50**, 1171–1178 (2007).
25. J.-Y. Raty, G. Galli, C. Bostedt, T. W. van Buuren, L. J. Terminello, Quantum confinement and fullerenelike surface reconstructions in nanodiamonds. *Phys. Rev. Lett.* **90**, 037401 (2003).
26. T. Irifune, A. Kurio, S. Sakamoto, T. Inoue, H. Sumiya, Ultrahard polycrystalline diamond from graphite. *Nature* **421**, 599–600 (2003).
27. H. Sumiya, T. Irifune, Hardness and deformation microstructures of nano-polycrystalline diamonds synthesized from various carbons under high pressure and high temperature. *J. Mater. Res.* **22**, 2345–2351 (2007).

28. C. D. Zuiker, A. R. Krauss, S. M. Gruen, J. A. Carlisle, L. J. Teminello, S. A. Asther, R. W. Bormett, Characterization of diamond thin films by core-level photoabsorption and UV excitation Raman spectroscopy. *Mat. Res. Soc. Symp. Proc.* **437**, 211 (1996).

29. R. W. Bormett, S. A. Asher, R. E. Witowski, W. D. Partlow, R. Lizewski, F. Pettit, Ultraviolet Raman spectroscopy characterizes chemical vapor deposition diamond film growth and oxidation. *J. Appl. Phys.* **77**, 5916 (1995).

30. M. J. Crane, B. E. Smith, P. B. Meisenheimer, X. Zhou, R. M. Stroud, E. J. Davis, P. J. Pauzauskie, Photothermal effects during nanodiamond synthesis from a carbon aerogel in a laser-heated diamond anvil cell. *Diamond Relat. Mater.* **87**, 134–142 (2018).

31. M. J. Crane, A. Petrone, R. A. Beck, M. B. Lim, X. Zhou, X. Li, R. M. Stroud, P. J. Pauzauskie, High-pressure, high-temperature molecular doping of nanodiamond. *Sci. Adv.* **5**, eaau6073 (2019).

32. P. J. Pauzauskie, J. C. Crowhurst, M. A. Worsley, T. A. Laurence, A. L. D. Kilcoyne, Y. Wang, T. M. Willey, K. S. Visbeck, S. C. Fakra, W. J. Evans, J. M. Zaug, J. H. Satcher Jr., Synthesis and characterization of a nanocrystalline diamond aerogel. *Proc. Natl. Acad. Sci. U.S.A.* **108**, 8550–8553 (2011).

33. H. K. Mao, J. Xu, P. M. Bell, Calibration of the ruby pressure gauge to 800 kbar under quasi–hydrostatic conditions. *J. Geophys. Res.* **91**, 4673–4676 (1986).

34. V. B. Prakapenka, A. Kubo, A. Kuznetsov, A. Laskin, O. Shkurikhin, P. Dera, M. L. Rivers, S. R. Sutton, Advanced flat top laser heating system for high pressure research at GSECARS: Application to the melting behavior of germanium. *High Press. Res.* **28**, 225–235 (2008).

35. A. F. Goncharov, V. B. Prakapenka, V. V. Struzhkin, I. Kantor, M. L. Rivers, D. A. Dalton, X-ray diffraction in the pulsed laser heated diamond anvil cell. *Rev. Sci. Instrum.* **81**, 113902 (2010).

36. J. Hafner, Ab-initio simulations of materials using VASP: Density–functional theory and beyond. *J. Comput. Chem.* **29**, 2044–2078 (2008).

37. P. E. Blöchl, Projector augmented-wave method. *Phys. Rev. B* **50**, 17953–17979 (1994).

38. J. P. Perdew, K. Burke, M. Ernzerhof, Generalized gradient approximation made simple. *Phys. Rev. Lett.* **77**, 3865–3868 (1996).

39. H. J. Monkhorst, J. D. Pack, Special points for Brillouin-zone integrations. *Phys. Rev. B* **13**, 5188–5192 (1976).